Spring 2014

APPLICATIONS OF CALCULATED SECOND HARMONIC GENERATION TENSORS ON MONOMOLECULAR AND BIMOLECULAR SYSTEMS

Gregory R. Snyder
Purdue University

Graduate School ETD Form 9
(Revised 12/07)

PURDUE UNIVERSITY
GRADUATE SCHOOL
Thesis/Dissertation Acceptance

This is to certify that the thesis/dissertation prepared

By Gregory R. Snyder

Entitled APPLICATIONS OF CALCULATED SECOND HARMONIC GENERATION TENSORS ON MONOMOLECULAR AND BIMOLECULAR SYSTEMS

For the degree of Master of Science

Is approved by the final examining committee:

Garth J. Simpson
Chair

Mary J. Wirth

Lyudmila Slipchenko

To the best of my knowledge and as understood by the student in the *Research Integrity and Copyright Disclaimer (Graduate School Form 20)*, this thesis/dissertation adheres to the provisions of Purdue University's "Policy on Integrity in Research" and the use of copyrighted material.

Approved by Major Professor(s): Garth J. Simpson

Approved by: R. E. Wild 4/15/2014
Head of the Graduate Program Date

APPLICATIONS OF CALCULATED SECOND HARMONIC GENERATION TENSORS ON MONOMOLECULAR AND BIMOLECULAR SYSTEMS

A Thesis

Submitted to the Faculty

of

Purdue University

by

Gregory R. Snyder

In Partial Fulfillment of the

Requirements for the Degree

of

Master of Science

May 2014

Purdue University

West Lafayette, Indiana

For my family

ACKNOWLEDGEMENTS

To Dr. Garth Simpson, words cannot do justice in expressing the gratitude I have for the rich learning experience you fostered for me over the past three years. From specific insights in nonlinear optics to the general qualities that make a better academic, I am thankful for everything that you have taught me. As a teacher, your patience and willingness to explain complicated concepts has enriched my experience at Purdue. As a mentor, your positive outlook on life and your open tolerance to questions has always made me feel invited. Never was there a time when I did not feel welcome in your group. As a scientist, the sheer and transparent excitement you show with your work has, and continues, to motivate me to become excited with mine. And as a friend, you have been a great person to hang out with over a drink. It has been a pleasure getting to know you.

To my committee members, Dr. Mary Wirth and Dr. Lyudmila Slipchenko, I am also especially thankful. To Dr. Wirth, your down-to-earth and pragmatic approach to how you share and present scientific information has served as a memorable model to me. To Dr. Lyudmila Slipchenko, I am grateful for all that I learned in computational chemistry, whether as a student or as a teaching assistant. Your instruction in classical simulations, along with former Simpson group member Dr. Levi Haupert's instruction in quantum chemistry, account for much of what I know today.

To the Simpson group, thank you for being a remarkable group of friends. It has been a pleasure getting to know each of you. The cutting edge work you do, and the rapid pace with which you do it, is a true benefit to mankind. To Azhad, it has been a pleasure working with you. The many exchanges we've had in regards to teaching general chemistry have been both enjoyable and insightful. To Ryan and Shane especially, I wish to express my thanks. Your words of advice, from the nuts and bolts of a particular project, to general communication in the scientific community, to even job hunting and the strategies involved in getting a position, have all been truly insightful. I could also not ask for a better pair of friends. Whether grabbing a bite to eat at the Nine Irish, or sharing our enthusiasm for video games and science fiction in the office, you have both contributed greatly to making me feel at home in West Lafayette. To each of you, and the rest of the Simpson group, I wish you the best in your careers. I have no doubt that you all will do great things.

To Mom, Dad, Michael, Daniel, Lara, Dana, and all my family, I cannot properly express the love and appreciation that I have for you. Whether standing by me during the moments when I needed you most, or simply being there to chat about anything and everything under the sun, you have seriously helped see me through these past three years. Talking to you about my work, sharing the experiences that I've had, and showing you around the town during your visits from Springfield have all been the highlights of this journey. Thank you. I could not be more blessed to have such an incredible family.

TABLE OF CONTENTS

Page

Page

LIST OF TABLES

LIST OF FIGURES

LIST OF ABBREVIATIONS

2D	two-dimensional
3D	three-dimensional
API	active pharmaceutical ingredient
GAMESS	general atomic and molecular electronic structure system
NLO	nonlinear optics
PDTPA	polarization-dependent two-photon absorption
SFG	sum frequency generation
SHG	second harmonic generation
SONICC	second order nonlinear optical imaging of chiral crystals
TAQ	2,6 di-tertbutyl-anthraquinone
TDHF	time-dependent Hartree Fock
TPA	two-photon absorption
TPEF	two-photon excited fluorescence
TPE-UVF	two-photon excited-ultraviolet fluorescence

ABSTRACT

Snyder, Gregory R. M.S., Purdue University, May 2014. Applications of Calculated Second Harmonic Generation Tensors on Monomolecular and Bimolecular Systems. Major Professor: Garth J. Simpson.

The field of nonlinear optics (NLO) has proven itself as a relatively recent and powerful area of science in the areas of microscopy and high-sensitivity quantification measurements. In particular, symmetry selective NLO processes such as second harmonic generation (SHG) take advantage of symmetry rules to cancel background noise almost completely, leading to both high resolution images and limits of detection (LOD) in the photon counting range. Background noise in SHG is negated as result of signal cancellation in systems containing inversion symmetry; generally isotropic sources. Quantum mechanical computational chemistry has enriched the field of NLO by enabling studies on hypothetical systems and environments that are otherwise unobtainable in experiments. Such systems are of benefit to study on account of their simplicity and the removal of common sources of experimental interference. In the presented work, three particular examples are presented. In the first example, simulated SHG response is investigated for noncentrosymmetric dimers constructed from nominally centrosymmetric monomers whilst a theoretical explanation is developed for the origin of said response. In the second example, calculated SHG tensor elements are used in a

sum-over-orientations algorithm to approximate experimentally bright SHG responses on various crystallized active pharmaceutical ingredients (APIs). By comparison with experiments, the predictive capability of time-dependent Hartree Fock (TDHF) is assessed with promising results. In the third example, SHG tensor elements calculated using TDHF simulations are utilized to predict polarization dependent two-photon absorption (PDTPA) for monomolecular systems. This is done by relating each SHG element to the product of the two-photon absorption element with the polarization dependent transition dipole.

CHAPTER 1 INTRODUCTION

1.1 Overview

The simplicity of simulated systems in nonlinear optics (NLO) is often a key incentive for studying them. By removing complications often seen in experiments, such as background noise, power variation in the laser, alignment errors in the instrument, and all the uncontrollable variables involved in sample preparation, the utility of computational chemistry to the field becomes apparent. But perhaps even more useful is the ability to study systems otherwise entirely unobtainable in real experiments. Such theoretical systems, even if never encountered in the laboratory, can still be of merit to study. For example, consider the observance of second harmonic generation (SHG) from noncentrosymmetric multimers constructed from nominally centrosymmetric monomers, the mechanism of which is still being explored and discussed today. Simulated experiments enable the study of systems as small as a single noncentrosymmetric dimer built from two small centrosymmetric molecules in vacuum. Such small systems are much easier to fully describe electronically with molecular orbital theory than the large, globular crystals actually observed in experiments. Of particular example is the single

dimer system consisting of two 1,3-butadiene molecules connected via pi stacking. The molecular orbital theory describing this system, and how it relates to a possible mechanism for SHG, is discussed in greater detail in chapter two.

Another type of simple and hypothetical system is the single unit crystallized active pharmaceutical ingredient (API). By utilizing algorithms provided by additional mathematical software (such as Mathcad), the relative SHG intensity for each API over a dynamic range can be predicted. Such algorithms include a sum-over-orientations calculation and how to take into account packing density via the cell volume. Further information regarding this approach, and how it impacts the drug development process, can be found in chapter three.

Finally, multiple types of computational calculations can be combined to predict molecular NLO properties previously unavailable to simulated experiments. For example, the use of SHG tensor elements and gamma tensor elements, along with their relationships to the molecular transition dipole and the two-photon absorption/emission matrices, can be exploited to calculate polarization-dependent two-photon absorption (PDTPA). More information on this topic can be found in chapter four.

Information in the following sections of chapter one provide further introduction on each of the three above mentioned simulated experiments, as well as the motivation behind them and how they can be applied to material science and drug development.

1.2 Organic Materials for Nonlinear Optical Applications

Monomers whose symmetry forbids SHG activity initially appear fruitless in the construction of new organic materials for nonlinear optical applications. But recent

experiments prove that bright SHG signal can come from systems consisting of nominally centrosymmetric monomers[1−5]. This is accomplished so long as the macromolecular system itself adopts a noncentrosymmetric arrangement. The exact mechanism which describes the observance of SHG from these systems is yet to be unambiguously determined. The related experiment attempts to provide evidence that exciton coupling between noncentrosymmetrically aligned conjugated bonds on the monomers is the correct mechanism.

One example of SHG arising from systems of nominally centrosymmetric monomers has been found in squaraines[1−5]. In this example, signal could be seen from analysis of Languir-Blodgett films built from centrosymmetric chromophores. In the actual system studied, each pair of monomers had formed a T-shaped dimer. The signal was attributed to intermolecular charge transfer between the two chromophores. This direct charge transfer was said to break the centrosymmetry of each individual monomer[6]. However, the actual structures of the squaraine multimers were not known, given the challenges of obtaining high-resolution structures of single monolayer organic films. While charge transfer alone can account for the observed SHG, this proposed mechanism cannot exclude alternative possible explanations. This is especially the case when lacking molecular information on the actual structures produced through said intermolecular interactions. Not all squairanes adopt T-shaped dimers, for example. Some adopt π-stacked systems[7], or π-stacked herring-bone structures[8] within the extended lattice.

Bright SHG can also be seen in H-aggregates of astaxanthin[9]. Astaxanthin is a type of centrosymmetric carotenoid. Each astaxinthin monomer is both rigid and centrosymmetric. The energetically stable crystal form for astaxinthin is also that of a centrosymmetric SHG-inactive lattice[10]. The lack of donor-acceptor-donor sites rules out direct or even partial charge-transfer as a viable mechanism for SHG.

In both previous examples, the observed SHG response for the multimer systems can be suggested to arise from intermolecular effects on the conjugated electronic motion of each monomer. Thus, it is reasonable to begin studies on an individual monomer unaffected by intermolecular forces from a nearby neighbor. Then exciton coupling theory can be introduced as a mechanism for the electronic structure perturbations and the resulting SHG[11−14].

The related experiment proposes and utilizes such a mechanism to justify nonzero SHG signal in noncentrosymmetric multimers constructed from centrosymmetric monomers. The specific system modelled consisted of simply two butadiene molecules in which one double bond was overlapped with the other to produce a 'Y' shaped dimer. Such a system was simple, computationally cheap, and suitable for providing a foundation for interpreting extended multimeric systems. Supplemental experimants on crystallized centrosymmetric 2,6-di-tertbutyl-anthraquinone (TAQ) via SHG microscopy were conducted to provide positive and negative controls and test predictions made by the exciton coupling mechanism. The results of the theory based experiment provide insights for predicting NLO properties of larger extended clusters and aggregates.

1.3 Application of an Algorithm for API Development

SHG microscopy is heavily utilized in the areas of chiral crystal detection and analysis. Due to inherent noise cancellation from inversion symmetry, the signal-to-noise ratio is high relative to other microscopy techniques. The result is a high selectivity for noncentrosymmetic crystals, overcoming the need for time-consuming signal-averaging. The assessment of crystallized APIs posits a particularly rich application for SHG microscopy. Crystalline properties, such as the rate of nucleation and the relative solubility in various temperatures and equilibria, is crucial when considering the development of new drugs. Crystallization of an API is necessary for determining its crystal structure, polymorphic forms, and stability.

Amorphous alternatives are also being increasingly utilized to promote drug solubility and bioavailability[15−18], creating a need to accurately determine the relative crystalline and amorphous content in a sample. By crystallizing the API under various temperatures, levels of humidity, and equilibria, the overall stability of the entire drug itself can be estimated. Due to zero signal from centrosymmetric media, SHG is both highly sensitive and highly selective for chiral crystals. Indeed limits of detection from SHG measurements are often many orders of magnitude lower than other common methods[19−20]. Thus, SHG microscopy is particularly useful in application to the pharmaceutical development process.

Nonetheless, some complications still exist. Chiral crystals of different APIs show remarkable variability in SHG response. This is mainly due to variable conjugated contributions from the electronic structure of each API; the main driving force behind the NLO process. Different crystalline geometries also play a contributing role. Different

levels of polymorphic mixing can also induce variety in SHG response for the same API, adding further complication. SHG active excipients also prove to be a regular problem.

Consequently, it is useful to know an API's approximate SHG *a priori.* A theoretical model for predicting an API's relative response is one possible solution. The related experiment calculates SHG tensor elements from time-dependent Hartree Fock (TDHF) in GAMESS of unit size chiral crystals of APIs. The calculation itself involves the determination of the second derivative of the API's polarizability with respect to an off resonance driving AC field. All modelled APIs, eighteen in total, were directly compared with SHG experiments. A good correlation in relative SHG response was observed between theory and experiment.

1.4 Polarization-Dependent Two-Photon Absorption from TDHF

Analytical theory was combined with time-dependent quantum chemical calculations to generate polarization-dependent nonlinear optical tensors, potentially addressing key limitations in alternative sum-over-states approaches. For more than a decade, even-ordered nonlinear optical techniques have been observed to be highly sensitive to chirality. Several possible origins of the chiral sensitivity have been suggested. However, many of the current approaches for calculating molecular hyperpolarizabilities do not easily or accurately recover the resonant response driving some of the most interesting measurements. Thus, an alternative approach has been described.

The derived analytical theory posits the hyperpolarizability tensor ($\chi^{(2)}$) as the kronecker product of the electronic transition dipole and the alpha matrix for two-photon

absorption over a frequency-dependent line shaped function. Each $\chi^{(2)}$ element can be decomposed into lower rank tensors, and this mathematical concept was exploited to show that certain ratios of different $\chi^{(2)}$ elements are approximately equal near resonance.

$\chi^{(2)}$ was calculated for gas-phase formaldehyde and tryptophan near the first resonance using TDHF simulations in general atomic and molecular electronic structure system (GAMESS) quantum mechanical software; the sign and values of the compared ratios were in good agreement for both molecules. A linear fit with the line shaped model was also applied to the formaldehyde $\chi^{(2)}$ elements in order to produce coefficients for the first six optically allowed resonances. The same ratios were taken with these coefficients, and the data was also found to be in good agreement.

Assuming that the nonlinear optical properties of a protein are dominated by the aromatic backbone, future studies beyond this experiment could include using an algorithm to predict polarization-dependent nonlinear optics of protein crystals.

1.5 References

1 Ashwell, G. J.; Williamson, P. C.; Bahra, G. S.; Brown, C. R., "2,4-bis 4-(dihexadecylamino)-2-hydroxyphenyl -squaraine: Second-harmonic generation from Langmuir-Blodgett monolayers of a centrosymmetric dye in which the chromophores are isolated from the substrate." *Australian Journal of Chemistry* **1999,** *52* (1), 37-41.

2 Honeybourne, C. L., "Charge distortion by sparkles can explain strong SHG by centrosymmetric squaraine dyes." *Journal of Materials Chemistry* **1999,** *9* (9), 2241-2244.

3 Ashwell, G. J.; Dyer, A. N.; Green, A.; Sato, N.; Sakuma, T., "Monolayer films of U-shaped molecules: suppression of the aggregation-induced second-harmonic generation of squaraine dyes by guest-host interactions." *Journal of Materials Chemistry* **2000,** *10* (11), 2473-2476.

4 Beverina, L.; Ruffo, R.; Patriarca, G.; De Angelis, F.; Roberto, D.; Righetto, S.; Ugo, R.; Pagani, G. A., "Second harmonic generation in nonsymmetrical squaraines: tuning of the directional charge transfer character in highly delocalized dyes." *Journal of Materials Chemistry* **2009,** *19* (43), 8190-8197.

5 Ashwell, G. J.; Jefferies, G.; Hamilton, D. G.; Lynch, D. E.; Roberts, M. P. S.; Bahra, G. S.; Brown, C. R., "STRONG 2ND-HARMONIC GENERATION FROM CENTROSYMMETRIC DYES." *Nature* **1995,** *375* (6530), 385-388.

6 Honeybourne, C. L., "A mechanism for strong SHG by centrosymmetric anilinosquaraine dyes." *Advanced Materials* **1999,** *11* (17), 1477-1480.

7 Beverina, L.; Crippa, M.; Salice, P.; Ruffo, R.; Ferrante, C.; Fortunati, I.; Signorini, R.; Mari, C. M.; Bozio, R.; Facchetti, A.; Pagani, G. A., "Indolic Squaraines as Two-Photon Absorbing Dyes in the Visible Region: X-ray Structure, Electrochemical, and Nonlinear Optical Characterization." *Chemistry of Materials* **2008,** *20* (10), 3242-3244.

8 Ashwell, G. J.; Bahra, G. S.; Brown, C. R.; Hamilton, D. G.; Kennard, C. H. L.; Lynch, D. E., "2,4-bis 4-(N,N-dibutylamino)phenyl squaraine: X-ray crystal structure of a centrosymmetric dye and the second-order non-linear optical properties of its non-centrosymmetric Langmuir-Blodgett films." *Journal of Materials Chemistry* **1996,** *6* (1), 23-26.

9 Tokarz, D. "Nonlinear Optical Properties of Carotenoid and Chlorophyll Harmonophores." University of Toronto, 2014.

10 Bartalucci, G.; Coppin, J.; Fisher, S.; Hall, G.; Helliwell, J. R.; Helliwell, M.; Liaaen-Jensen, S., "Unravelling the chemical basis of the bathochromic shift in the lobster carapace; new crystal structures of unbound astaxanthin, canthaxanthin and zeaxanthin." *Acta Crystallographica Section B-Structural Science* **2007,** *63*, 328-337.

11 Simpson, G. J.; Perry, J. M.; Moad, A. J.; Wampler, R. D., "Uncoupled oscillator model for interpreting second harmonic generation measurements of oriented chiral systems." *Chem. Phys. Lett.* **2004,** *399*, 26-32.

12 Perry, J. M.; Moad, A. J.; Begue, N. J.; Wampler, R. D.; Simpson, G. J., "Electronic and vibrational second-order nonlinear optical properties of protein secondary structural motifs." *J. Phys. Chem. B* **2005,** *109*, 20009-20026.

13 Gualtieri, E. J.; Haupert, L. M.; Simpson, G. J., "Interpreting nonlinear optics of biopolymer assemblies: Finding a hook." *Chem. Phys. Lett.* **2008,** *465*, 167–174.

14 Wanapun, D.; Wampler, R. D.; Begue, N. J.; Simpson, G., J., "Polarization-Dependent Two-photon Absorption for the Determination of Protein Secondary Structure: A Theoretical Study." *Chem. Phys. Lett.* **2008,** *455*, 6-12.

15 N. Jagadeesh Babu, A. N., Solubility Advantage of Amorphous Drugs and Pharmaceutical Cocrystals. *Cryst. Growth Des.* **2011,** *11*, 2662-2679.

16 Parks, B. C. H. a. M., What is the True Solubility Advantage for Amorphous Pharmaceuticals? *Pharmaceutical Research* **1999,** *17* (4), 397-404.

17 Thayer, A. M., Form and Function. *Chemical and Engineering News* 2007, pp 17-30.

18 Thayer, A. M., Finding Solutions. *Chemical and Engineering News* 2010, pp 13-18

19 Wanapun, D.; Kestur, U. S.; Taylor, L. S.; Simpson, G. J., Single Particle Nonlinear Optical Imaging of Trace Crystallinity in an Organic Powder. *Anal. Chem.* **2011,** *83* (12), 4745-4751.

20 Wanapun, D.; Kestur, U. S.; Taylor, L. S.; Simpson, G. J., Quantification of trace crystallinity in an organic powder by nonlinear optical imaging: Investigating the effects of mechanical grinding on crysallinity loss. *Abstracts of Papers of the American Chemical Society* **2011,** *241*.

CHAPTER 2 EXCITON COUPLING INDUCED SHG IN DIMERS

2.1 Introduction

Second Harmonic Generation (SHG) signal observed from systems built from nominally centrosymmetric molecular units can be interpreted using the simple exciton coupling model. A relatively straightforward example was shown using the single hypothetical butadiene dimer held together via overlapping conjugated bonds. Time-dependent Hartree-Fock (TDHF) calculations of the nonlinear polarizability of the dimer were attributed to this model based on the electronic structure of the monomer and the relative orientation between the monomers. Experiments on a sample of centrosymmetric 2,6 di-tertbutyl-anthraquinone (TAQ) gave evidence for a mixture of crystals both SHG-active and SHG-inactive. The dominant form is centrosymmetric, structurally known, and SHG-inactive. The various metastable impurities are SHG-active and are likely arranged in noncentrosymmetric molecular configurations not too different from the hypothetical butadiene dimer.

2.2 Theoretical Framework

Molecular orbital theory can be used to assist in the interpretation of SHG-activity via exciton coupling. In particular, the work utilized the molecular orbital diagram for the 1,3-buadiene dimer. For nominally centrosymmetric molecules, it is well established that all vibrational and electronic transitions are exclusively one-photon or two-photon allowed, but never both simultaneously. Each molecular second harmonic generation tensor, $\beta^{(2)}$, is simply described by the product of the two-photon transition matrices α and the one-photon transition moments μ. It should be clear, then, that in systems which are either exclusively one-photon or two-photon allowed, every nonlinear tensor must go to zero value. This is especially clear given the equation below. This description only holds when the incident energy is near half the resonance an electronic transition.

$$\beta^{ijk}\left(-2\omega;\omega,\omega\right)=\sum_{n}S_{n}\left(2\omega\right)\mu_{0n}^{i}\alpha_{n0}^{jk} \tag{1}$$

Eq. 1 also only holds for systems in the ground state. The frequency (ω) dependent S_n is a line-shaped function, and is complex valued. It can be described as follows:

$$S_{n}\left(2\omega\right)=\frac{1}{\hbar}\cdot\frac{1}{\omega_{n}-2\omega-i\Gamma_{n}} \tag{2}$$

ω_n corresponds to resonant frequency between the ground state and any given excited state. The last term in the denominator is the damping constant.

Adding together all of the monomer excited states gives the corresponding dimer states. However, to have a good approximation, only those monomer states that are closest in energy need be considered.

$$\Psi_{d}=\sum_{m}c_{m}\left(\psi_{m}^{1}\mp\psi_{m}^{2}\right) \tag{3}$$

Figure 2-2 gives the actual molecular orbital diagram describing the linear combination of monomer orbitals to get the dimer orbitals. Each exciton state in the dimer can be described by the sums and differences of the one-photon transition moments and the two-photon matrices from each corresponding monomer transition. If each *g* dimer state is only described by the monomer states *g1* and *g2*, and each *u* dimer state is only described by the monomer states *u1* and *u2*, then there should still be no SHG signal expected from the dimer. This is again due to one-photon and two-photon exclusivity and taking into account Eq. 1. However, if the *g* dimer states are allowed even minor contribution from the monomer *u* states, and dimer *u* states are allowed minor contribution from the dimer *g* states, then it becomes clear that SHG signal is enabled. These minor contributions are described by Eq. 3. Essentially, it is the mixing of two-photon absorption character (even if relatively minor) into one-photon allowed monomer transitions and vice versa, which enable the observance of SHG signal in the dimer.

2.3 Results of the Simulation

Before considering the butadiene dimer, it is useful to start with a review of the electronic structure of the monomer. Butadiene conforms to the C_{2h} point group, which is centrosymmetric and SHG-inactive by symmetry. Based on quantum chemical calculations, the two lowest energy transitions correspond to a π-π^* HOMO-LUMO transition of B_u symmetry, with the next highest energy transition corresponding to B_g symmetry. As required by symmetry in centrosymmetric molecules, each transition must be allowed for either one-photon or two-photon excitation, but not both. In this case, the B_u transition is one-photon allowed and two-photon forbidden, while the B_g state is one-

photon forbidden and two-photon allowed. Quantum chemical calculations of the butadiene monomer confirm these expectations, even when symmetry is not rigorously imposed.

When positioned in a π-stacking configuration such as shown in Figure 2-1, the symmetry of the dimer becomes C_2, with the *A* and *B* states generated from linear combinations of the monomer states. Because of the odd symmetry of the π-orbitals, the difference states are lower in energy than the sum states in π-stacked dimers, consistent with the exciton coupling diagram depicted in Figure 2-2.

The exciton coupling model of a dimer is fully rigorous in the limit of inclusion of all excited states in the summation. In brief, the set of excited states serves as a basis set for recovering the new states in the coupled system. Since the excited states themselves are constructed from a linear combination of fundamental basis set functions, so too are the states produced from exciton coupling. In the limit of weak coupling consistent with intermolecular interactions (as opposed to covalent bond formation), each exciton state of a dimer can be reasonably described by the interactions between just one or two excited states of the monomer. However, the practical need to consider a finite number of excited state couplings can potentially introduce uncertainties in the approach. Consequently, the approach is likely to be most accurate when the coupling between monomers is relatively weak (such that only a few excited states are required to recover the exciton states) and for molecular systems with a relatively sparse population of spectrally overlapping excited states capable of participation in coupling. These are both reasonable assumptions in the present case.

Unlike the C_{2h} point group, the *A* and *B* states of the dimer can in principle each be both one-photon and two-photon allowed. However, in practice the core nature of the monomer transitions is carried over when describing the excited state transitions in the dimer arising from exciton coupling. Within the validity of this simple exciton coupling description, the most significant contributions to the dimer states will be produced from the sums and differences of the corresponding orbitals of the monomers. For example, considering just the two excited state transitions shown in Figure 2-2, the one-photon transition moment to the first excited B state should be recovered from the vector difference between the two monomer transition moments, resulting in predominantly *y*-polarized transition with an oscillator strength equal to the *y*-component of the monomer multiplied by √2.

The total wavefunction describing the lowest excited state transition in the dimer can be written as a linear combination of both the major one-photon allowed B_u contributions and the minor two-photon allowed B_g contributions.

$$\Psi_B = c_{B_u}\left(\psi^1_{B_u} - \psi^2_{B_u}\right) + c_{B_g}\left(\psi^1_{B_g} - \psi^2_{B_g}\right); c_{B_u} > c_{B_g} \tag{4}$$

The corresponding transition moments as well as the matrices describing two-photon absorption can be similarly produced from appropriately weighted sums and differences.

$$\begin{aligned} \mu_B &= c_{B_u}\left(\mu^1_{B_u} - \mu^2_{B_u}\right) + c_{B_g}\left(\mu^1_{B_g} - \mu^2_{B_g}\right) = c_{B_u}\left(\mu^1_{B_u} - \mu^2_{B_u}\right) \\ \alpha_B &= c_{B_g}\left(\alpha^1_{B_g} - \alpha^2_{B_g}\right) \end{aligned} \tag{5}$$

Although $c_{B_u} > c_{B_g}$, the presence of a nonzero contribution from the B_g transition provides some two-photon transition character that can drive nonzero values of the

hyperpolarizability tensor $\beta^{(2)}$. In this simplified three-state model for the monomer, the hyperpolarizability tensor for the lowest-lying *B* state is approximated by the following expression.

$$\beta_B^{ijk} = S_B(2\omega)\mu_B^i\alpha_B^{jk} \cong S_B(2\omega)c_{B_u}\left(\mu_{B_u}^1 - \mu_{B_u}^2\right)^i \cdot c_{B_g}\left(\alpha_{B_g}^1 - \alpha_{B_g}^2\right)^{jk}; c_{B_u} > c_{B_g} \quad (6)$$

The corresponding tensor contributions for the *A* states is given by the summation (rather than the difference) between the monomer μ and α terms.

This model suggests several specific predictions that can be compared directly with computational and experimental results. First, that the dominant tensor elements driving the hyperpolarizability in the dimer can be predicted based on the symmetries of the corresponding monomer states contributing to exciton coupling. Second, that in the limit of weak inter-chromophore coupling, the SHG-activity should approach zero. Third, that the SHG-activity of the dimer should be substantially enhanced close to resonance, but approach zero far from resonance. And finally, that significant charge transfer is not expected for the observation of SHG-activity in the dimer.

The first prediction follows directly from the analysis exemplified in Eq. 6. The second is clear conceptually, but potentially less so mathematically. In the limit of weak coupling, the excited state energies of an exciton pair converge to nearly degenerate values. In this limit, it becomes nearly mathematically equivalent to describe the dimer in a basis set consisting of two uncoupled monomers rather than as a coupled dimer. The key criterion has already been established for assessing whether the hyperpolarizability can be considered through the coherent summation of two uncoupled monomers, or if coupling and exciton state descriptions are required. Specifically, coupling should be

considered if the energy splitting is comparable or greater than the experimental linewidth of the transition, and can safely be neglected under conditions in which it is not.

The third prediction is closely related to the second. From inspection of Eq. 2, the weighting of each exciton state in the net hyperpolarizability is related to the energy difference between the exciton state and $2\hbar\omega$, where ω is the fundamental frequency. As the second harmonic frequency moves away from resonance, the contribution from each of the exciton states approaches a single constant. For example, the two exciton transition moments from the pair of B_u monomer states each contribute with approximately equal weight, such that the net result is closely approximated by the direct coherent sum of the uncoupled monomers. Correspondingly, in this limit far from resonance the perturbation from exciton coupling becomes negligible.[1,2] Since the unperturbed system of two centrosymmetric monomers is SHG-inactive, the nonresonant result should also converge to that same outcome far from resonance.

The fourth prediction is quite straightforward. Since neither of the monomers possesses a net dipole nor charge transfer character in any of the transitions, little or no charge transfer is expected in the exciton states produced from sums and differences of those same monomer states.

The predictions of the exciton coupling model were compared with the results of quantum chemical calculations of the linear and nonlinear optical properties of the butadiene monomer as a point of reference for interpreting the NLO properties of the dimer structures. CIS calculations for the monomer were performed and are summarized briefly in the Supporting Information. In brief, the lowest lying excited state corresponds

to a transition of B_u symmetry, consistent with the presence of a transition moment polarized within the *xz* plane using the coordinate system indicated in Figure 2-2. The next highest excited state is one-photon forbidden, suggesting either A_g or B_g symmetry. The symmetry is tentatively assigned as B_g based on trends in the dimer detailed below.

The butadiene structure considered computationally was one in which just one pair of carbon atoms were coparallel and π-stacked, as shown in Figure 2-2. In this configuration, the butadiene dimer has C_2 symmetry. A summary of the linear optical properties of the dimer is provided in the Supporting Information.

As a simple confirmatory test, the hyperpolarizability as a function of intermolecular separation is shown in Figure 2-3. As one might expect, the magnitude of each hyperpolarizability tensor element uniformly decreases as the intermolecular distance is increased, asymptotically approaching a value of zero in the limit of negligible inter-chromophore coupling consistent with the second prediction of the exciton coupling model.

The hyperpolarizability tensor elements as a function of fundamental wavelength are summarized in Figure 2-4. Results for the frequency-dependent dimer calculations clearly demonstrate a trend in which the beta tensor elements are rapidly reduced in magnitude as the incident wave is shifted further from resonance. Again, this observation is in good agreement with the predictions of the exciton coupling model.

Interestingly, the largest magnitude for the SHG-activity is given in the "chiral" β_{zxy} tensor element with the largest relative enhancement close to resonance. The dominance of this contribution can be understood within the context of the exciton coupling model by considering just the two lowest excited states in the butadiene

monomer. The monomer B_u (HOMO-LUMO) transition is polarized within the *yz*-plane of the chromophore and oriented largely along the long *z*-axis of the molecule. The lowest energy B-exciton state in the dimer should be formed from the difference of the two monomer wavefunctions (given the sign difference between the *p*-orbitals), with symmetry dictating that it be *y*-polarized, and with a transition moment roughly $\sqrt{2}$ larger in magnitude than the monomer, in excellent agreement with the quantum chemical calculations. Similarly, the next highest excited state in the dimer should consist of the sum of the monomer wavefunctions, corresponding to an A-state with a *z*-polarized transition moment. The major contributions to this pair of A and B states will arise from coupling primarily from just the two one-photon allowed monomer B_u states. However, the dimer A and B states can also borrow minor contributions from the next highest two-photon allowed excited state of B_g symmetry. For a transition of B_g symmetry, the nonzero TPA tensor elements in the monomer will be α_{xy} and α_{xz}, the first of which can contribute exclusively to A-states in the dimer, and the second exclusively to B-states.

Combining the nonzero elements of μ and α according to Eq. 1, the lowest energy dimer transition should be dominated by the β_{yxz} tensor element (nonzero μ_y and borrowed α_{xz}), and the next highest transition dominated by the β_{zxy} tensor element (large μ_z and borrowed α_{xy}). Given the larger one-photon transition moment along the long monomer *z*-axis, it is not surprising that the second excited state in the dimer corresponding to the β_{zxy} tensor element drives much of the NLO activity near resonance.

These combined conditions predict relatively large contributions from the "chiral" tensor elements, in reasonably good agreement with the computational results. The tensor elements β_{zyx} and β_{yxz} are larger in magnitude than all other tensor elements (at all three

wavelengths considered). For example, the next most significant tensor element was β_{zzz}, presumably arising from the large μ_z from the B_u monomer transition coupled with α_{zz} contributions from the next higher excited states of B_g symmetry.

The steep sensitivity of the calculated hyperpolarizability with fundamental wavelength indicated in Figure 2-3 is noteworthy. This trend is consistent with the molecular orbital diagram depicted in Figure 2-2, assuming the "borrowing" of the one-photon and two-photon contributions goes both ways in this two-excited state limit. While the lowest two excited states of the dimer yield nonzero values for β_{yxz} (nonzero μ_y and borrowed α_{xz}) and β_{zxy} (large μ_z and borrowed α_{xy}), the next highest exciton pair will similarly be driven largely by equal and opposite contribution to those same tensor elements β_{yxz} (borrowed μ_y and nonzero α_{xz}) and β_{zxy} (borrowed μ_z and nonzero α_{xy}). The requirement that they sum to approximately zero in the two-excited state model arises simply by nature of the centrosymmetry of the monomers from which the dimer states were generated. Of course, additional excited states are also present and contributing, but the general sensitivity to resonance-enhancement in the dimer can still be qualitatively understood within the context of this argument.

2.4 Results of the Experiment

Crystals of TAQ form a particularly useful benchmark to test the exciton coupling model. The particular set of nonzero tensor elements generated from exciton coupling depend solely on the relative orientation, and not their relative position.[3] The magnitudes of the tensor elements are affected by the degree of coupling, but not which tensor elements are nonzero. Consequently, the allowed tensor elements are arguably most

easily identified by considering first structures for the TAQ dimer with different relative positions between the monomers. Based on a previously published crystal structure, TAQ forms a centrosymmetric, SHG-inactive crystal structure of $P_{\bar{1}}$ symmetry, in which every monomer is in exactly the same orientation within the lattice and each monomer is centrosymmetric.[4] Considering a dimer formed from two monomers of identical orientation, the wavefunctions for the sum states will simply be identical but rescaled, and all the difference states will be zero-valued. As such, the SHG activity of the TAQ dimer and crystal is interesting to interpret within the context of the exciton coupling model. Considering a dimer comprised of two monomers offset in space by not rotated, the symmetry of the dimer is formally C_i and should result in no SHG activity.

In SHG measurements of TAQ powders as received (Figure 2-5), the large majority (92.6% of the total area) was SHG-inactive as expected based on the known crystal form. Consequently, the absence of significant SHG from the large majority of the TAQ powder is in excellent agreement with both the established bulk crystal symmetry and the exciton coupling arguments.

Since the established crystal structure for TAQ material is symmetry-forbidden for SHG,[26] it is particularly noteworthy that strong SHG is nevertheless observed from localized domains within the powdered sample. While the large majority of the TAQ powder is SHG-inactive consistent with expectations, approximately 7.4% of the total area in Figure 2-5a is occupied by SHG-active domains, representing a small but significant total volume fraction of the material. The SHG activities of the TAQ crystals rival those of $BaTiO_3$, used as a reference material. Recrystallization by rapid

desolvation resulted in a ~10-fold increase in the integrated SHG activity of the TAQ powder per unit area, shown in Figure 2-5d.

Following recrystallization, the SHG-active TAQ crystals were placed in a sealed container with a saturated vapor pressure of 1,4-dioxane (the solvent used in the initial crystallization), then re-imaged after 3 days at room temperature (Figure 2-5e, 2-5f). Over this time-frame, the SHG activity of the sample within the same field of view was reduced 27-fold to levels similar to those observed initially within the crystalline powder.

The observation of such a reduction in SHG from an identical region of the powder strongly suggests the absence of bulk-allowed quadrupolar or magnetic dipole origins for the observed SHG signals. Both higher-order effects arise with comparable efficiency irrespective of the presence or absence of centrosymmetry in the bulk. As such, their contributions would be unlikely to be perturbed by the solvent-mediated recrystallization. This observation is in noteworthy contrast to vibrational SFG measurements of the benzene/air interface, in which calculations and measurements suggest quadrupole effects may be significant.[5,6] Furthermore, SHG arising from trace impurities can similarly be excluded, as they would be present in equal quantities before and after exposure to solvent vapor. In addition, the SHG intensity produced by TAQ rivals that of the noncentrosymmetric bulk dipole-allowed $BaTiO_3$ reference, which strongly suggests a bulk-allowed electric dipole origin if the observed signal.

Given the steep dependence on the preparation method, the SHG arising from the TAQ following recrystallization is attributed to the production of at least one alternative new noncentrosymmetric crystal form. In previous studies, it has been shown that rapid solvent evaporation can promote the formation of metastable polymorphs by placing

crystallization under kinetic control rather than thermodynamic control.[7,8] The observed loss in SHG activity shown in Figure 2-5 following exposure of the crystals to solvent vapor is in good agreement with this explanation, as adsorbed solvent films can facilitate the interconversion between different crystalline solvates and/or polymorphs.[9]

Two possible mechanisms for the observed bright SHG-activity within the TAQ crystals are considered. First, intermolecular interactions could be distorting TAQ to break the molecular inversion symmetry. This mechanism can be excluded by inspection of the structure of TAQ, which consists of a rigid ring with significant flexibility only in the t-butyl rotation angles. It is unlikely that the relatively weak intermolecular interactions driving crystal packing will substantially distort the centrosymmetric ring structure driving the nonlinear polarizability of TAQ. It is equally unlikely that a noncentrosymmetric eclipsed configuration for the t-butyl groups as opposed to the centrosymmetric staggered configuration would exhibit substantially enhanced nonlinear optical activity of the monomer. Consequently, the observation of SHG activity is attributed to intermolecular exciton coupling interactions within a noncentrosymmetric lattice.

It is interesting that the regions of high SHG in TAQ were brighter than the $BaTiO_3$ reference materials. Given that the molecular building block is forbidden by symmetry to produce SHG, such bright signals are clear indicators of intermolecular interactions within the lattice as a key driving influence. The influence of these interactions is likely further increased through resonance-enhancement. The low lying transitions in TAQ approach energies correspond to the twice the incident photon energy, while $BaTiO_3$ is transparent throughout the visible spectrum.

The presence of an SHG-active form for the TAQ crystals is in excellent qualitative agreement with the exciton coupling model described herein. While the packing arrangement within this new polymorph is not yet established, for the present purposes it is sufficient to note that it is clearly and strongly SHG-active, despite being produced from a centrosymmetric molecular building block.

2.5 References

1 Wanapun, D.; Wampler, R. D.; Begue, N. J.; Simpson, G., J., "Polarization-Dependent Two-photon Absorption for the Determination of Protein Secondary Structure: A Theoretical Study." *Chem. Phys. Lett.* **2008,** *455*, 6-12.

2 Haupert, L. M.; Simpson, G. J., "Chirality in Nonlinear Optics." *Annu. Rev. Phys. Chem.* **2009,** *60*, 345–65.

3 Franz, A. W.; Rominger, F.; Muller, T. J. J., "Synthesis and Electronic Properties of Sterically Demanding N-Arylphenothiazines and Unexpected Buchwald−Hartwig Aminations." *The Journal of Organic Chemistry* **2008,** *73* (5), 1795-1802.

4 Muir, R. D.; Kissick, D. J.; Simpson, G. J., "Statistical connection of binomial photon counting and photon averaging in high dynamic range beam-scanning microscopy." *Optics Express* **2012,** *20* (9).

5 Matsuzaki, K.; Nihonyanagi, S.; Yamaguchi, S.; Nagata, T.; Tahara, T., "Vibrational Sum Frequency Generation by the Quadrupolar Mechanism at the Nonpolar Benzene/Air Interface." *Journal of Physical Chemistry Letters* **2013,** *4* (10), 1654-1658.

6 Kawaguchi, T.; Shiratori, K.; Henmi, Y.; Ishiyama, T.; Morita, A., "Mechanisms of Sum Frequency Generation from Liquid Benzene: Symmetry Breaking at Interface and Bulk Contribution." *J. Phys. Chem. C* **2012,** *116* (24), 13169-13182.

7 Hall, V. J.; Simpson, G. J., "Direct Observation of Transient Ostwald Crystallization Ordering from Racemic Serine Solutions." *Journal of the American Chemical Society* **2010,** *132* (39), 13598-13599.

8 Chowdhury, A. U.; Dettmar, C. M.; Sullivan, Z. S.; Zhang, S.; Harden, S. E.; Jacobs, K. T.; Ingram, N.; Kissick, D. J.; Wanapun, D.; Maltais, T.; Simpson, G. J., "Kinetic trapping of metastable amino acid polymorphs." *submitted*.

9 Giron, D.; Goldbronn, C.; Mutz, M.; Pfeffer, S.; Piechon, P.; Schwab, P., "Solid state characterizations of pharmaceutical hydrates." *Journal of Thermal Analysis and Calorimetry* **2002,** *68* (2), 453-465.

Table 2-1 CIS calculations on butadiene monomer and dimer. Each monomer transition gives rise, through addition and subtraction, to two dimer transitions.

	Monomer	Dimer (8.0 A)	Dimer (3.8 A)
1st excited state	Energy: 198.2 nm μ_x = 0 Debye μ_y = -1.37 Debye μ_z = 6.47 Debye Symmetry: Bu	Energy: 199.8 nm μ_x =0.01 Debye μ_y = -1.92 Debye μ_z = 0 Debye Symmetry: B	Energy: 211.1 nm μ_x = -0.02 Debye μ_y = 1.76 Debye μ_z = 0 Debye Symmetry: B
		Energy: 196.9 nm μ_x = 0 Debye μ_y = 0 Debye μ_z = 9.04 Debye Symmetry: A	Energy: 193.8 nm μ_x = 0 Debye μ_y = 0 Debye μ_z = -6.90 Debye Symmetry: A
2nd excited state	Energy: 190.9 nm μ_x = 0 Debye μ_y = 0 Debye μ_z = 0 Debye Symmetry: Bg	Energy: 191.4 nm μ_x = 0 Debye μ_y = -0.09 Debye μ_z = 0 Debye Symmetry: B	Energy: 193.2 nm μ_x = 0.11 Debye μ_y = -0.26 Debye μ_z = 0 Debye Symmetry: B
		Energy: 191.3 nm μ_x = 0 Debye μ_y = 0 Debye μ_z = -0.21 Debye Symmetry: A	Energy: 187.9 nm μ_x = 0 Debye μ_y = 0 Debye μ_z = 3.77 Debye Symmetry: A
3rd excited state	Energy: 181.0 nm μ_x = 0.79 Debye μ_y = 0 Debye μ_z = 0 Debye Symmetry: Au	Energy: 181.1 nm μ_x = 0 Debye μ_y = 0 Debye μ_z = -0.01 Debye Symmetry: A	Energy: 182.8 nm μ_x = 0 Debye μ_y = 0 Debye μ_z = 3.72 Debye Symmetry: A
		Energy: 181.1 nm μ_x = 1.18 Debye μ_y = 0 Debye μ_z = 0 Debye Symmetry: B	Energy: 182.2 nm μ_x = -2.21 Debye μ_y =0 Debye μ_z = 0 Debye Symmetry: B

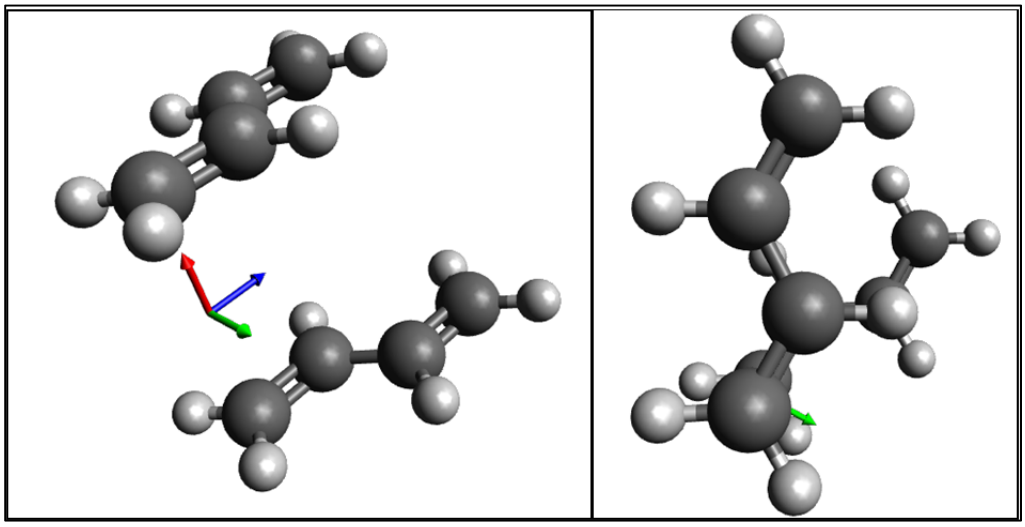

Figure 2-1 Butadiene dimer images. 1,3-butadiene dimer used in quantum simulations, arranged so that the z-axis is the primary axis of rotation. The z-axis is blue, the x-axis is red, and the y-axis is green. The monomers are stacked on top of each other to form a 'Y' shape as can be seen from the top-down view of the second image. The distance between the monomers is 3.8 Å, which matches the π-stacking distance between the aromatic rings in the crystal structure used in the companion paper.

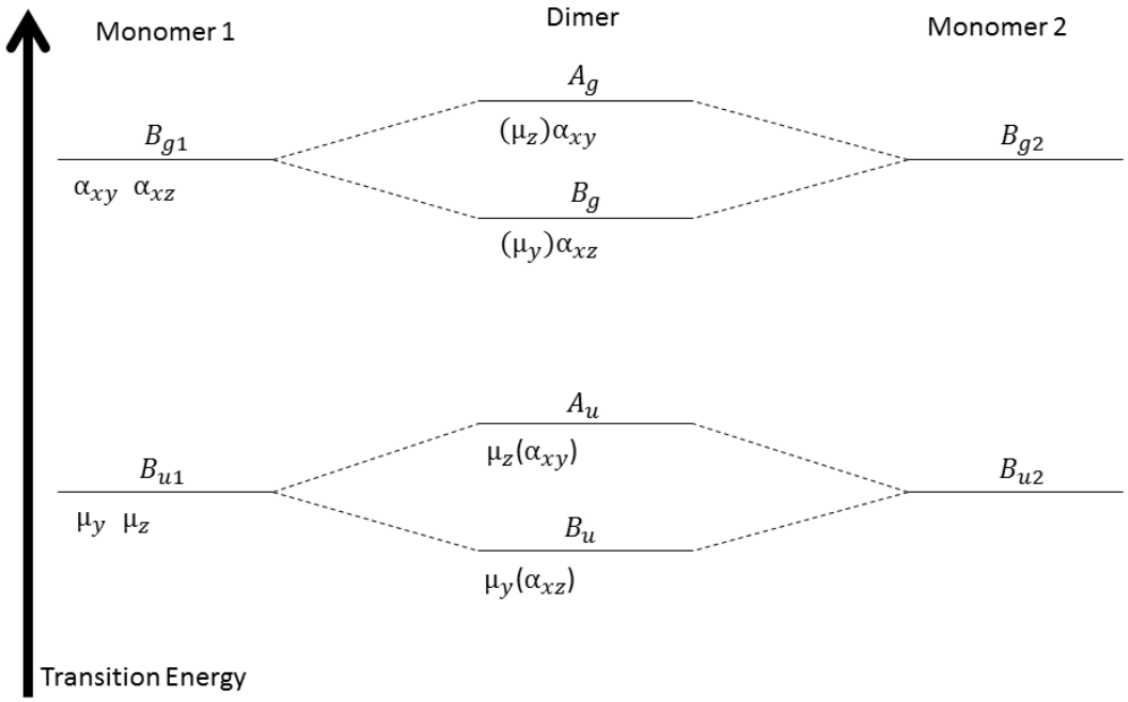

Figure 2-2 Exciton coupling diagram for 1,3-butadiene. Terms in parenthesis represent relatively small contributions from a different dimer transition. Such overlap in molecular orbitals is allowed due to similar symmetry.

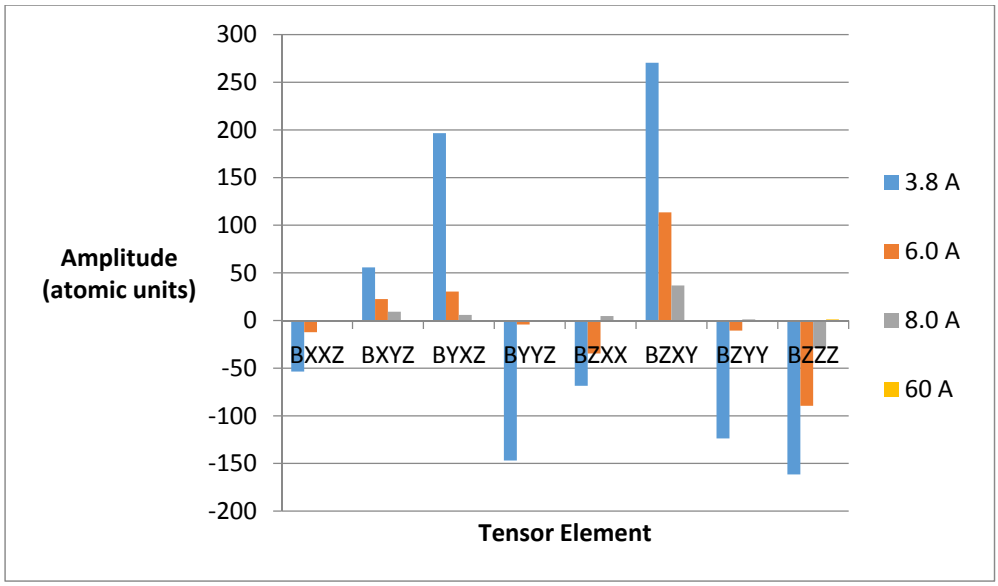

Figure 2-3 Calculated hyperpolarizability of 1,3-butadiene dimer at varying dimer distances. All calculations were performed at 450 nm.

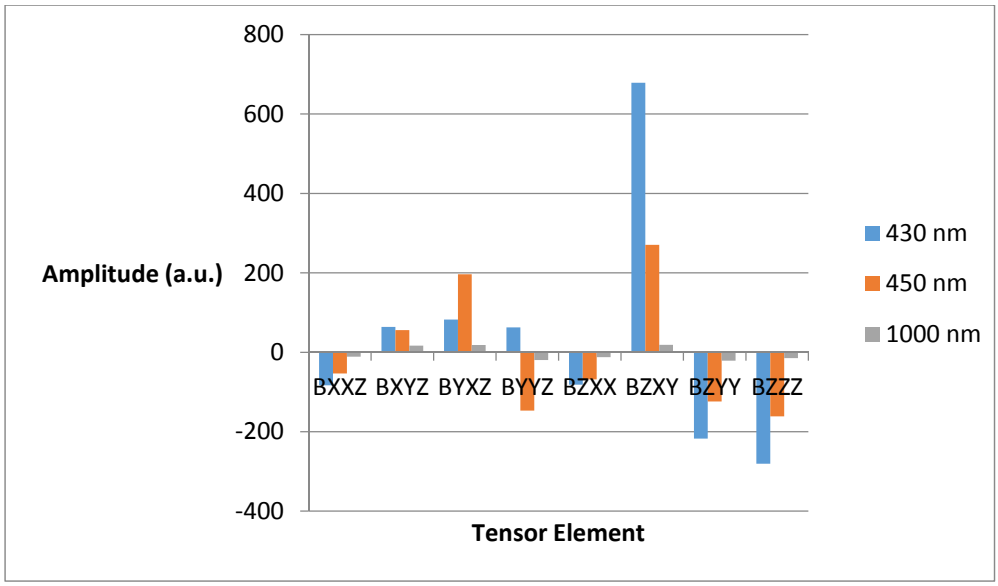

Figure 2-4 Calculated hyperpolarizability of the 1,3-butadiene dimer at different incident frequencies. All calculations were performed at a dimer separation of 3.8 Å.

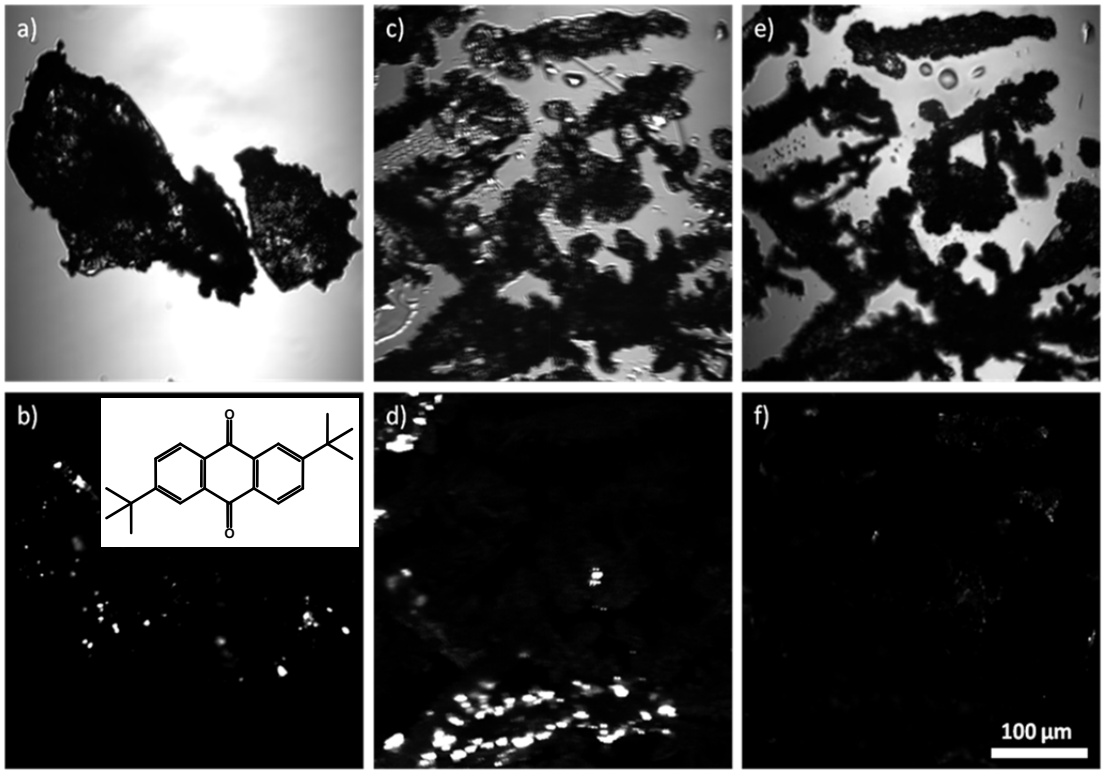

Figure 2-5 Laser transmitted images of TAQ. Different crystallization conditions are presented (top row) along with the corresponding SHG images (bottom row). The chemical structure of TAQ is also shown in the inset. Figure a) and b) correspond to the powder as received, c) and d) correspond to the crystals grown by the solvent evaporation over the time course of a few minutes, e) and f) are the images of the same sample following enclosure in a chamber containing high solvent vapor pressure for three days. The SHG images are all presented using a common intensity scale relative to a $BaTiO_3$ nanoparticle reference.

CHAPTER 3 PREDICTED SHG OF API CRYSTALS FROM SHG TENSORS

3.1 Introduction

A model for predicting the anticipated second harmonic generation (SHG) activity of active pharmaceutical ingredient (API) crystals was developed based on combining time-dependent Hatree-Fock calculations of the molecular building block with analytical theory for the predicted intensity from the lattice. Predicted trends agreed well overall with experimental measurements of 18 representative APIs. Inspection of the SHG images suggest that outliers from the predicted trends likely arose either from the presence of trace SHG-active metastable crystal forms not considered in the predictions or from relatively poor crystallinity within the sample. The success of this relatively simple computational approach suggests a route for reliably predicting the anticipated SHG activities of API target molecules, which in turn can serve to indicate their potential compatibility with analysis by SHG.

3.2 Computational Algorithim and Experimental Confirmation

All calculations were done using the General Atomic and Molecular Structure System (GAMESS)[1,2] quantum chemical package. Each hyperpolarizability calculation was performed using time-dependent Hartree Fock (TDHF) using a restricted Hartree Fock self-consistent field with a 6-311G basis set including d and p heavy atom polarization functions and diffuse L-Shell on heavy atoms. The incident energy for all calculations was chosen to be 0.043 Hartrees, corresponding to the 1060 nm incident beam used in the experiments. Unmodified atomic geometry coordinates were obtained from the Cambridge Structural Database (CSD).[3] Avogadro[4] software, version 1.0.3, was used to convert the files to GAMESS input cards. Chimera NLOPredict[5] was used for the tensor evaluations and visualizations. Calculations were performed on the following molecules with TDHF: benzocaine, captopril, clarithromycin, D-(-)Salicin, dexamethasone, efavirenz, flutamide, griseofulvin, itraconazole, ketoconazole, loratadine, mevastatin, naproxen, quinidine, tacrolimus, tadalafil, tolazamide, and triamcinolone.

From the molecular tensors, the $\chi^{(2)}$ tensors of the crystals were estimated by performing the symmetry operations of the lattice as described previously.[6,7] In both studies, the bulk crystal NLO properties were approximated by averaging the orientations of the individual molecular tensors and then taking their coherent sum. A graphical illustration of this process is shown in Figure 3-1 for the $P_{2_1 2_1 2_1}$ lattice of captopril.In the case of the $P_{2_1 2_1 2_1}$ crystal of captopril in Figure 3-1, three orthogonal C_2 rotations were performed about the three principal axes. Although the symmetry operations formally correspond to combinations of both rotation and translation, the translation distance is

much less than the wavelength of light and can reasonably be neglected in the analysis. Each individual panel is a visual hyper-ellipsoid representation of the molecular $\beta^{(2)}$ tensor, the length of which corresponds to the magnitude of the β_{zzz} projection along that direction in space and the color of which indicates the sign of the emerging field (red = negative, blue = positive).[8] Coherent summation of the four different captopril orientations present within the lattice leads to the net response indicated to the right in the figure. In addition to the hyper-ellipsoid representation, a complementary vector-sphere representation is also show. Whereas the hyper-ellipsoid only indicates the projection onto the normal of the sphere, the vector-sphere recovers the polarization direction of the nonlinear field and is therefore a more complete map. Finally, the tensor was then scaled based on crystal packing density by simply dividing by the unit volume to produce the crystal $\chi^{(2)}$ susceptibility.

The instrument utilized for sample analysis is a commercially-available Formulatrix SONICC system powered by a Fianium FemtoPower laser, 1060 nm, capable of producing 1.3 W, 51 MHz repetition rate, and a 166 fs pulse width. Multiple models of this instrument are available, with various detector configurations. The model utilized in this study collected SHG light in the transmission direction, and two-photon excited UV fluorescence (TPE-UVF) light in the refelected (epi) direction, with the latter generated by passing the 1060 nm light through a lithium triborate doubling crystal prior to the sample, generating 530 nm light. While theoretical TPE-UVF activities were not calculated, the collection of TPE-UVF data was prudent for several reasons, including: aiding in the analysis of outliers, experimental demonstration of an equally large dynamic

range for TPE-UVF, and the relative ease of obtaining additional data given the automation of the measurements on the commercial platform.

Sample preparation can significantly influence the degree of scattering of both the incident laser and the signal that is generated. The samples were sieved resulting in a particle size range between 106-250 μm (tacrolimus and tadalafil were not sieved due to limited sample quantity and cost constraints). Once sieved, the powdered samples were placed between two glass cover slips and filled to the tops of binder reinforcement rings, allowing for uniform sample thickness. Four replicates of each sample were prepared, and within each sample three spots were examined for a total of 12 replicate measurements per API. Due to the variability of sample and sample-holder positioning, a 1 mm distance in the z-direction (parallel to beam propagation) was probed in 40 μm steps to ensure the entire sample was imaged. Vendors for all compounds measured are listed in the supplementary information.

Due to the inherent variability in both the SHG and fluorescence activities of APIs, multiple acquisition profiles were necessary to remain within the linear dynamic range of the photon counting hardware used. The incident laser powers at the sample along with acquisition times are listed in Table 3-1 for each unique acquisition profile. The instrument utilizes beam-scanning at ~8 kHz, allowing for higher incident laser powers while also mitigating sample damage. The laser was focused onto the sample with a pseudo-10x objective providing a 500 x 500 μm field of view, corresponding to 512 8-bit pixels on each axis.

Each field of view for the data collected was averaged and stacked (NIH ImageJ). The z-plane for each sample corresponding to the greatest signal intensity was averaged with two z-planes above and below. An average signal intensity for each API was generated by averaging all 12 replicates. Also reported are the 95% confidence intervals.

3.3 Results and Reliability of the Algorithm in Predicting SHG Signal of APIs

A comparison of the predicted and measured SHG activities of 18 representative APIs is shown in Figure 3-2. The experimentally-determined SHG activity spanned a range of 7 decades, from loratadine (dimmest) to flutamide (brightest). All results were normalized to the signal of flutamide, as it was observed to have the highest SHG activity. In general, good agreement was found between the predicted and observed SHG activities of the different APIs. In most instances, the *ab initio* calculations with no adjustable parameters were within and order of magnitude of the experimental observations from relatively complex mixtures of powders. Given the many factors that affect the observed SHG activity and the relative simplicity of the analytical model, the recovery of such good agreement across 7 decades of variation in signal is especially encouraging.

Experimental data for the same API provided in Figure 3-1 (captopril) is provided in Figure 3-3. The brightfield image (Figure 3-3a) with a field of view of 500 x 500 um, and the corresponding SHG image (Figure 3-3b), along with the TPE-UVF image (Figure 3-3c). A 3d rendered threshold image utilizing multiple z-planes and NIH ImageJ was utilized to generate Figure 3-3d. A line trace of the SHG image from Figure 3-3b is provided in Figure 3-3e providing the SHG intensity as a function of distance in one axis.

The ketoconazole, efavirenz, and itraconazole samples were all racemates with centrosymmetric lattices, with the theoretical response therefore simply set to the dark noise limit of the instrument. However, the experimental results produced relatively weak but clearly detectable localized SHG. Closer inspection of the images for these three compounds suggest the presence of SHG-active puncta corresponding to a small volume fraction of noncentrosymmetric material present. The sparse but nonzero SHG activity is tentatively attributed to the presence of trace homochiral crystals present within the mixture. Recent studies of metastable homochiral crystallization from racemic solutions supports the relative ease with which such unfavored crystal forms can be routinely produced.[9] This argument is further supported by the much weaker SHG response observed from crystals of the achiral molecule loratadine, which occupies a centrosymmetric C_{2c} space group and has no viable pathway to produce metastable homochiral crystal forms.

Tadalafil and (D)-(-) salicin also represent two interesting outlying cases worthy of additional discussion. Images for D-(-)-salicin are provided in the Supporting Information and suggest the API was not fully crystalline. As shown in Figure 3-3, the TPE-UVF and SHG images are generally expected to overlay reasonably well in crystalline materials that exhibit both SHG activity and detectable UV fluorescence. However, the two sets of images for salicin exhibited significant regions with relatively bright TPE-UVF signals and negligible SHG activity. Qualitatively similar results although not as pronounced were also observed in the case of tadalafil, also shown in the Supporting Information. Therefore, the large disparity between the predicted and

observed SHG response of these two APIs is tentatively attributed to poor crystallinity within the samples.

A range of measured SHG and TPE-UVF activities for diverse representative APIs and select excipients is provided in Figure 3-4. This expanded list helps place the API's used for quantum chemical calculations within the scope of the broader set of anticipated SHG activities. It is interesting to note that the diversity in SHG activities spanning ~7 decades is roughly comparable to the span of signals observed using TPE-UVF. Furthermore, little correlation between the two signals was observed, as the two processes arise from fundamentally different physical effects. This independence is easily illustrated by the different behaviors between griseofulvin (bright for both methods) and flutamide (among the brightest for SHG and weakest for TPE-UVF).

Reasonable agreement between the measured SHG activities and those predicted based on *ab initio* TDHF calculations was observed for several representative APIs. The seven-decade measured dynamic range of SHG activities observed for different APIs can complicate *a priori* prediction of the appropriateness of a target for SHG analysis and/or the selection of instrument setting consistent with the anticipated signal levels. This computational framework can provide a starting point for initially estimating the anticipated SHG activities of small molecule crystals based on known or assumed crystal structures. Experimental outliers in which signals above predictions were observed in racemic solids from unanticipated SHG-active domains are tentatively attributed to homochiral metastable crystal forms. Based on comparisons between SHG and TPE-UVF images, two instances of significant over-estimation of the anticipated SHG activity (tadalafil and salicin) were attributed to the presence of poorly crystalline or amorphous

API content. The reasonably good overall agreement between theory and experiment generally suggest the validity of the computational approach, while also providing a fairly straightforward strategy for estimating the anticipated SHG-activities of new small-molecule candidate crystals.

3.4 References

1 General Atomic and Molecular Electronic Structure System" M.W.Schmidt, K.K.Baldridge, J.A.Boatz, S.T.Elbert, M.S.Gordon, J.H.Jensen, S.Koseki, N.Matsunaga, K.A.Nguyen, S.Su, T.L.Windus, M.Dupuis, J.A.Montgomery J. Comput. Chem., 14, 1347-1363(1993).

2 Advances in electronic structure theory: GAMESS a decade later" M.S.Gordon, M.W.Schmidt pp. 1167-1189, in "Theory and Applications of Computational Chemistry: the first forty years" C.E.Dykstra, G.Frenking, K.S.Kim, G.E.Scuseria (editors), Elsevier, Amsterdam, 2005.

3 F. H. Allen, Acta Cryst., B58, 380-388, 2002 "The Cambridge Structural Database: a quarter of a million crystal structures and rising".

4 Marcus D Hanwell, Donald E Curtis, David C Lonie, Tim Vandermeersch, Eva Zurek and Geoffrey R Hutchison; "Avogadro: An advanced semantic chemical editor, visualization, and analysis platform" *Journal of Cheminformatics* **2012**, 4:17

5 UCSF Chimera--a visualization system for exploratory research and analysis. Pettersen EF, Goddard TD, Huang CC, Couch GS, Greenblatt DM, Meng EC, Ferrin TE. *J Comput Chem.* 2004 Oct;25(13):1605-12.

6 Zyss, J.; Oudar, J. L., Relations between microscopic and macroscopic lowest-order optical nonlinearities of molecular crystals with one- or two-dimensional units. *Phys. Rev. A* **1982,** *26*, 2028-2048.

7 Wampler, R. D.; Begue, N. J.; Simpson, G., J., Molecular Design Strategies for Optimizing the Nonlinear Optical Properties of Chiral Crystals. *Cryst. Growth and Design* **2008,** *8*, 2589-2594.

8 Wampler, R. D.; Moad, A. J.; Moad, C. W.; Heiland, R.; Simpson, G., J., Visual methods for interpreting optical nonlinearity at the molecular level. *Acc. Chem. Res.* **2007,** *40*, 953-960.

9 Chowdhury, A. U.; Dettmar, C. M.; Sullivan, Z. S.; Zhang, S.; Harden, S. E.; Jacobs, K. T.; Ingram, N.; Kissick, D. J.; Wanapun, D.; Maltais, T.; Simpson, G. J., Kinetic trapping of metastable amino acid polymorphs. *submitted*.

Table 3-1 Laser power vs collection time for API SHG and fluorescence. All of the incident laser powers (at sample) and collection times used to that ensure signals generated were within the dynamic range of the data acquisition cards, highlighting the large variation in observable signal intensities from APIs.

SHG	**Fluorescence**
449 mW, 1.8 s	260 mW, 0.45 s
250 mW, 1.8 s	150 mW, 0.45 s
150 mW, 0.45 s	50 mW, 0.45 s
74 mW, 0.45 s	25 mW, 0.45 s
	5 mW, 0.45 s

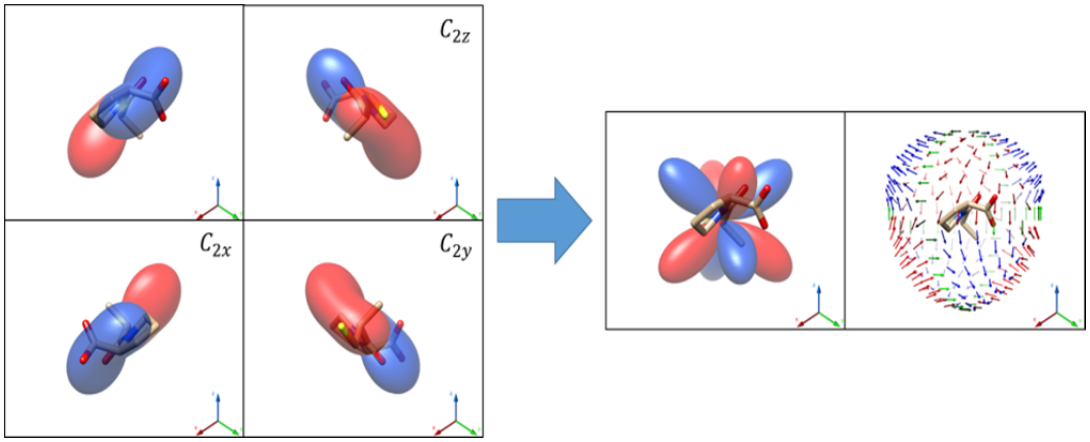

Figure 3-1 Hyperellipsoid representation of an API $\chi^{(2)}$tensor. The tensor magnitude for each individual panel was scaled down by a factor of 15 relative to the sum on the right for clarity.

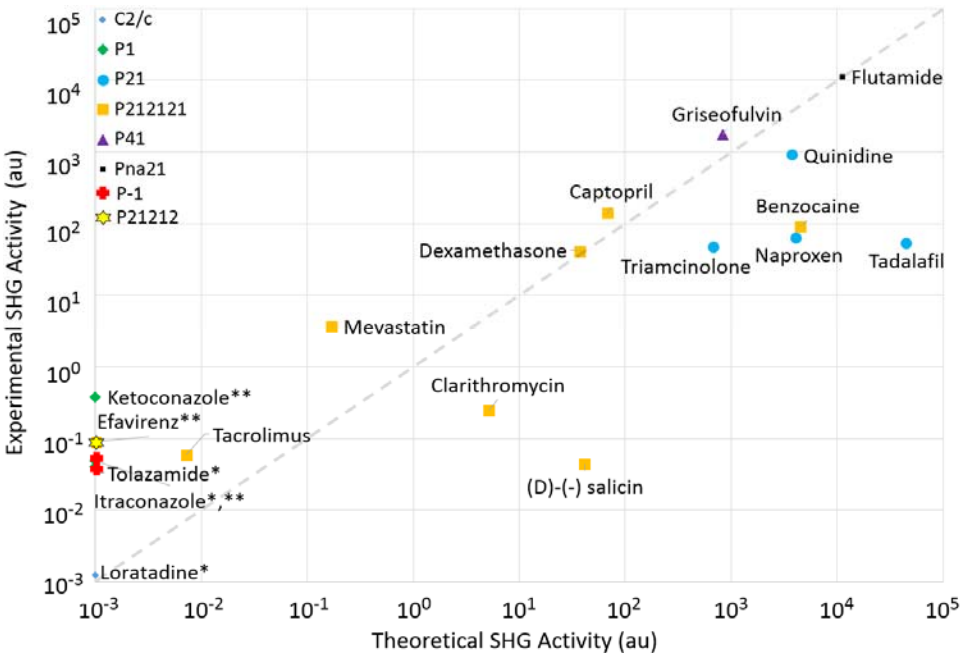

Figure 3-2 Comparison between theory and experiment for known API structures. The dotted line on the diagonal is shown to visualize perfect agreement between experiment and theory. *Denotes a centrosymmetric crystalline space group, **denotes a racemic crystalline form.

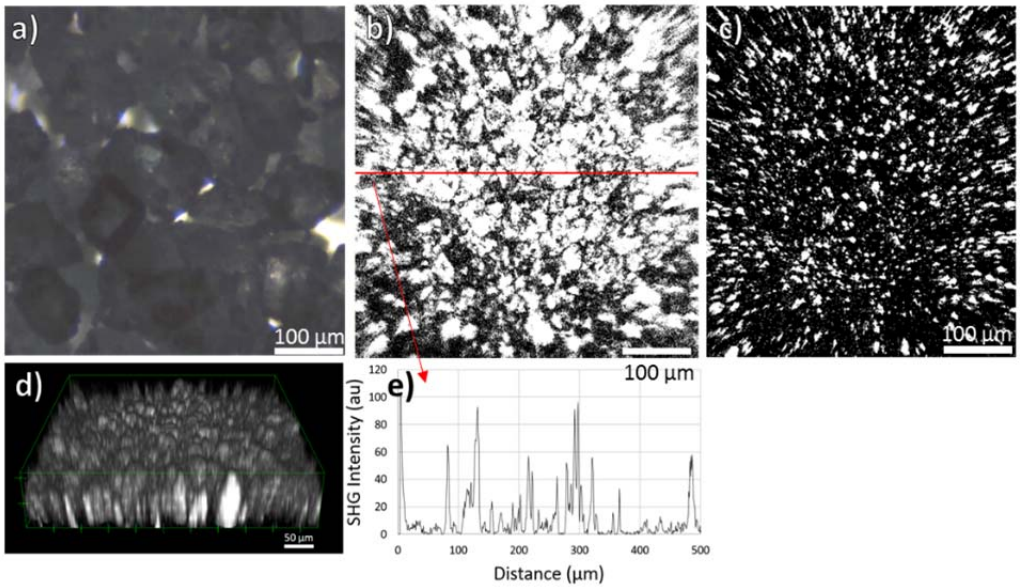

Figure 3-3 Imaging data for API captopril. a) Brightfield image. b) Corresponding SHG image, with 3d representation in d) and line trace (red) found in e), and c) a 2d TPE-UVF image of the same FOV.

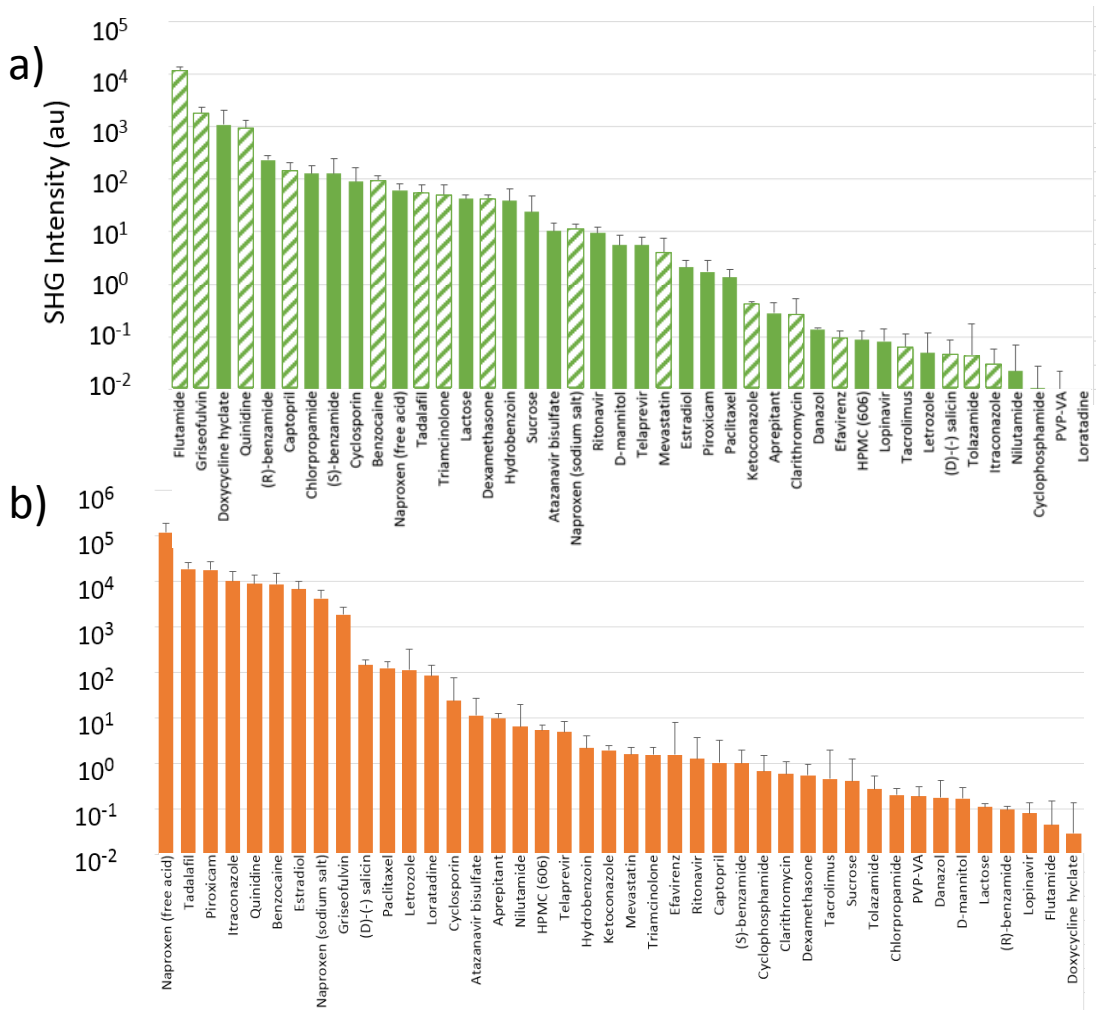

Figure 3-4 Comparison of SHG and TPE-UVF activities for each API. A) Observed relative SHG activities of all 42 compounds studied. Compounds are listed in order of decreasing SHG activity, with dashed bars denoting compounds for which TDHF was performed. B) Observed relative TPE-UVF activities of the same compounds.

CHAPTER 4 PDTPA FROM TDHF CALCULATED SHG TENSORS

4.1 Introduction

Time-dependent Hartree Fock (TDHF) can produce individual polarization-dependent tensor elements for any incident frequency. Such tensor elements can be used to indirectly calculate polarization-dependent two-photon absorption (PDTPA). As of current, there is no reliable computational package available for obtaining PDTPA. A sum-over-states approach has been utilized in the past[1−4]. This approach involves the sum of contributions from hundreds of states. Unfortunately there exists a high sensitivity to the basis sets used in the calculation and relatively poor reproducibility can serve as a significant barrier for some systems. A newer, and perhaps more promising approach, involves the use of TDHF calculations to determine the beta and gamma tensor elements; and then applying a new theoretical equation to take certain ratios of tensor elements which result in ratiometric two-photon absorption values. This new approach has first been demonstrated on the simple system formaldehyde. The long-term objective is to be able to use the nonlinear optical (NLO) properties of a single dominant amino acid to produce the NLO properties of an entire gas-phase protein, and then from there, determine the NLO properties of isotropic protein and/or protein crystals.

4.2 PDTPA From Beta and Gamma Tensors

Two main questions are addressed using the general atomic and molecular electronic structure system (GAMESS) TDHF calculations regarding hyperpolarizabilities of formaldehyde, and how higher order tensor elements (beta, gamma) can be broken down into products of alpha tensors and transition moments near resonance. The first main question postulates that beta (second harmonic generation) tensor elements are equal to the product of the transition moment and alpha for two-photon absorbance. In other words, the following equation holds true:

$$\beta_{abc} = Line(\omega) * \mu_a \alpha_{bc} \quad (1)$$

In Eq. 1, μ_a is the polarized transition moment, α_{bc} is the two-photon absorption amplitue, and a, b, and c are any direction of polarizability. Line(ω) is a line shaped sum function that contains the incident frequency dependence and contribution from each resonance. An established model for this function is:

$$Line(\omega) = \sum_{n=1,2\ldots m}^{m} \frac{1}{\omega_n - 2\omega + \Gamma} \quad (2)$$

In Eq. 2, ω_n is a resonance frequency, and Γ is a dampening factor. This line shape function is consistent with the resonance enhancement observed in experiments. As half the incident frequency approaches a resonance, the line shaped function will quickly increase to infinity in value, causing the measured β_{abc} signal to also increase to near infinity. The second main question postulates that gamma (TPA and TPE) is equal to the product of the two two-photon matrices. In other words, that the following equation holds true:

$$\gamma_{abcd} = Line(\omega) * \alpha_{ad}\, \alpha_{bc} \quad (3)$$

In Eq. 3, a, b, c, and d are orthogonal directions of polarizability, $Line(\omega)$ is the frequency-dependent line shaped function, α_{ad} is the two-photon emission amplitude, and α_{bc} is the two-photon absorption amplitude.

Since GAMESS TDHF calculations are parametric, the TPA matrix cannot be calculated directly. But certain ratios of second order tensor elements can be taken to verify the above mentioned equations. For example, imagine taking the ratio of β_{xyy}/β_{xzz}. This would give the following expression:

$$\frac{Line(\omega)*\mu_x\alpha_{yy}}{Line(\omega)*\mu_x\alpha_{zz}} \quad (4)$$

If ω is taken to be near resonance, then it becomes apparent that the line shaped functions will cancel, on account that the dominant contributing resonance cancels. The polarized transition moments also cancel, leaving a ratio of alpha two-photon absorption amplitudes, α_{yy}/α_{zz}. In a similar fashion, certain ratios of alpha two-photon absorption amplitudes can be indirectly determined from gamma calculations. For example, taking the ratio of $\Upsilon_{xyyx}/\Upsilon_{xzzx}$ to get the following equation:

$$\frac{Line(\omega)*\alpha_{xx}\alpha_{yy}}{Line(\omega)*\alpha_{xx}\alpha_{zz}} \quad (5)$$

Again, terms cancel, leaving a ratio of alpha two-photon absorption amplitudes, α_{yy}/α_{zz}. These equations can be verified by comparing any two beta tensor ratios which give the same ratio of TPA amplitudes and confirming that the values are nearly the same. Data mentioned further in this chapter demonstrates this confirmation.

Figure 4-1 is a graph plotted for β_{xxx}over the range from 800 nm to 10 nm in 10 nm increments.

Any energy higher than 350 nm results in complete divergence in all tenser elements. The divergence is likely due to the location of the first resonance predicted by TDHF at about 175 nm. For reference, all the provided data in the listed tables are taken at 380 nm incident wavelength. Note how the plot does not oscillate. This is an apparent contradiction to the line shaped function, which would predict an increase as the as the incident frequency approaches the first resonance, then decrease as it passes over, then increase again when reaching the second resonance, and so on. The reason for the lack of oscillation can be attributed to the fact that the locations of the resonances are relatively close to each other, and continue to become closer for higher frequencies. The oscillations are in fact there, but they are buried, but possibly can be recovered by a linear fit.

Figure 4-2 is a plot of the ratio of beta tensor element values which cancel to give a ratio of two-photon absorption amplitudes near resonance. Where the plot flattens corresponds to a resonance. Near resonance the line shaped functions cancel (on account of being dominated by a single pathway), enabling the ratio of alpha two-photon absorption amplitudes to be relatively frequency-independent.

In Table 4-1, each row corresponds to changing only the first index in the beta tensor element, which according to the mentioned theory, changes only the polarized dipole moment in the numerator and denominator in Eq. 4. But since the polarized dipole moment in the numerator and in the denominator always match, they should always cancel, consistently leaving the ratio of alpha two-photon absorption amplitudes (ie, XX/XY, in the first row). As can be seen in Table 4-1, beta tensor values are very

consistent within a single row, as predicted. These values also agreed well with polarized transitions taken from a CIS calculation, showing further internal consistency.

Due to the fact that multiple pathways will compete off resonance, it is expected that these ratios do not agree for off-resonance measurements. Some brief data was taken to confirm this, with measurements taken at 500 nm, which is much below the first electronic resonance energy, and this was found to be the case.

Eq. 5 can also be verified in the similar manner of testing for consistency among certain calculated gamma tensor ratios. For example, the ratio can be taken to give the following expression:

$$\frac{\gamma_{ijkh}}{\gamma_{ilmh}} = \frac{Line(\omega)*\alpha_{ih}\alpha_{jk}}{Line(\omega)*\alpha_{ih}\alpha_{lm}} = \frac{\alpha_{jk}}{\alpha_{lm}} \quad (6)$$

Again, the line shaped function will only cancel for near resonance measurements, due to domination by one pathway. The alphas for two-photon emission (*ih*) should cancel as well, leaving only the ratios for two photon absorption amplitudes (*jk* and *lm*). In Table 4-2, it is shown that again, internal consistency is observed. For example, row one describes the polarization dependent ratio of two photon absorption amplitudes α_{xx}/α_{yy}, and it is observed that row one is consistent regardless of what is chosen for polarization dependent two photon emission. It can also ensured that the same alpha ratios calculated from taking gamma and beta ratios match each other, demonstrating further internal consistency. For example,

$$\frac{\gamma_{iaai}}{\gamma_{ibbi}} = \frac{Line(\omega)*\alpha_{aa}}{Line(\omega)*\alpha_{bb}} = \frac{Line(\omega)*\mu_i\alpha_{aa}}{Line(\omega)*\mu_i\alpha_{bb}} = \frac{\beta_{iaa}}{\beta_{ibb}} = \frac{\alpha_{aa}}{\alpha_{bb}} \quad (7)$$

For near resonance measurements, all the line functions cancel. In the case of gamma ratios, the alpha two photon emission amplitudes cancel, and in the case of beta

ratios, the polarized transition moments cancel – leaving the same $\frac{\alpha_{aa}}{\alpha_{bb}}$ value in both expressions. This is observed when comparing $\frac{\alpha_{xx}}{\alpha_{yy}}$, for example. The value is near -37 when calculated, regardless if it is derived from the beta or the gamma calculations.

4.3 Resonance Dependent Beta Coefficients from a Linear Fit

Recent work is now focused on fitting the measured data of formaldehyde (and soon tryptophan) to a linear fit in hopes of recovering resonance dependent beta coefficients. Mathcad was used to make the fit, and the data was fit to the following equation:

$$\beta(data) = \sum_{n=1,2\ldots m}^{m} \frac{\beta(coefficient)_n}{\omega_n - 2\omega} * \omega^4 \qquad (8)$$

The ω^4 term is to account for photon scattering, and the dampening term Γ is omitted. The resonances were determined from a Time Dependent Density Function Theory (TD-DFT). The only adjustable parameters are the resonance dependent beta coefficients, and so it is a linear fit. A single fit corresponds to a particular set of orientations for three wave mixing (SHG), such as x in, y in, y out. This fit allows the farming of the polarization and resonance dependent second order nonlinear response of the sample. Two ways to test how well the algorithm is working is to see how well the fitted data fits the measured data, as well as whether or not we see good internal agreement when taking ratios of the determined beta coefficients, such that the transition moments cancel to give alpha two photon absorption amplitude ratios (now at each resonance). Although good internal agreement was observed among the coefficient ratios, the linear fit is something were still having trouble with. For example, observe the

fitted data for β_{xxx} for three wave mixing.. As can be seen in Figures 4-3 and 4-4, the attempt to fit such huge magnitude values in the higher frequency range causes massive deviations between the fit and the data in the lower frequency range. Below is the same fit plotted only to 0.1 hartrees for clarification.

Although the internal agreement among the fit coefficients (that give the same alpha two photon absorption values) are encouraging, the failure to produce a good fit to the measured data suggests that something is wrong with the model. Alternative models are currently being studied in an attempt to give a better fit. One such model adds a dampening factor represented by a square function. Another possible model includes a dampening factor that is represented by the fuorier transform of a one-sided exponential. These alternative models were the next in line to be studied.

4.4 References

1 Zhang, M.-y.; Li, G.-S.; Li, L.-P., First-principles study of one and two-photon absorption of an artificial fluorescent protein chromophore by 5-hydroxytryptophan substitution. *Chem. Phys. Letters*, **2013**, *588, 220-225*

2 Zhang, Min-Yi; Xu, Can; Lin, Chen-Sheng; Guan, Xiangfeng; Cheng, Wen-Dan, Theoretical study of the proton transfer wires influence on the one- and two-photon absorption properties of green fluorescent protein chromophore. *Org. & Bio. Chem.,* **2013**, *11, 1414-1422*

3 Zhao, Yang; Guo, Jing-Fu; Ren, Ai-Min; Feng, Ji-Kang, Theoretical study of one- and two-photon absorption properties of pyrene derivatives. *Theoretical Chem. Accounts,* **2011**, *128, 265-274*

4 Neves, U. M.; De Boni, L.; Ye, Zhihong; Bu, Xiu R.; Mendonca, C. R., Two-photon absorption spectra of Salen dye complexes with azo dyes. *Chem. Phys. Letters,* **2007**, *441, 221-225*

Table 4-1 Formaldehyde SHG tensor elements. Comparison of 27 unique Beta tensor elements calculated on Formaldehyde using TDHF. Incident energy at 380 nm.

	i = X	Y	Z
iXX/iXY	-11.1862	-11.1852	-11.1853
iXX/iYY	-37.469	-37.4317	-37.4684
iYY/iXY	0.298546	0.298817	0.298527
iXX/iXZ	-11.6537	-11.6543	-11.6536
iXX/iZZ	-1.02737	-1.02733	-1.02737
iZZ/iXZ	11.3433	11.34422	11.34321
iYY/iYZ	-0.13904	-0.13918	-0.13904
iYY/iZZ	0.027419	0.027446	0.02742
iZZ/iYZ	-5.07102	-5.07104	-5.0708

Table 4-2 Formaldehyde gamma tensor elements. Comparison of several unique Gamma tensor elements calculated on Formaldehyde using TDHF. Incident energy at 380 nm.

	i = X	Y	Z
iXXi/iYYi	-37.4681	-37.4591	-37.4673
iXXi/iZZi	-1.02737	-1.02735	-1.02736
iYYi/iZZi	0.02742	0.027426	0.02742

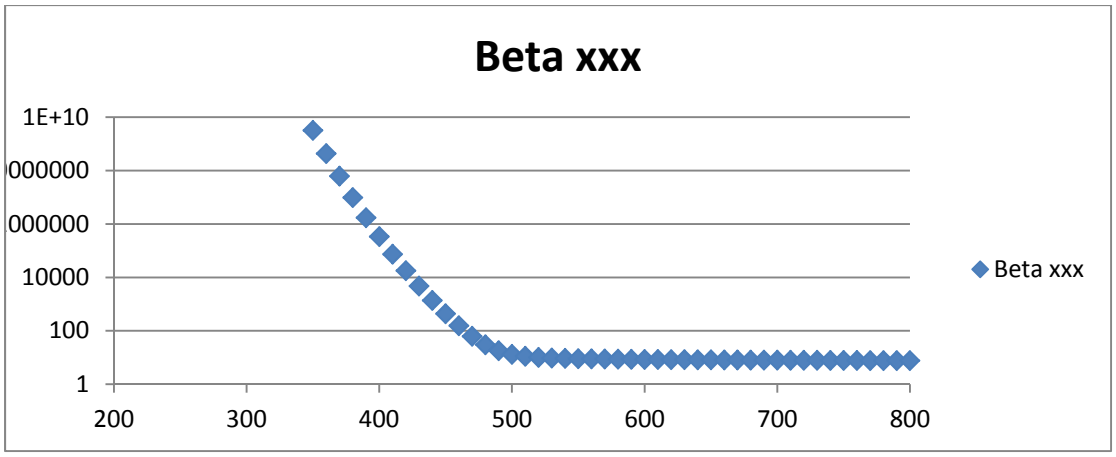

Figure 4-1 Beta xxx vs incident frequency.

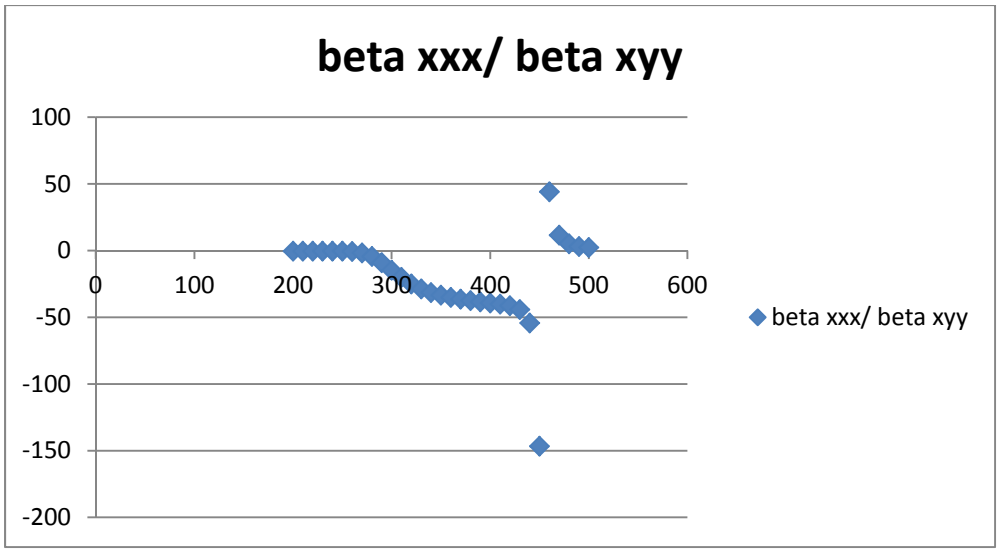

Figure 4-2 Ratio of beta tensor elements vs incident frequency.

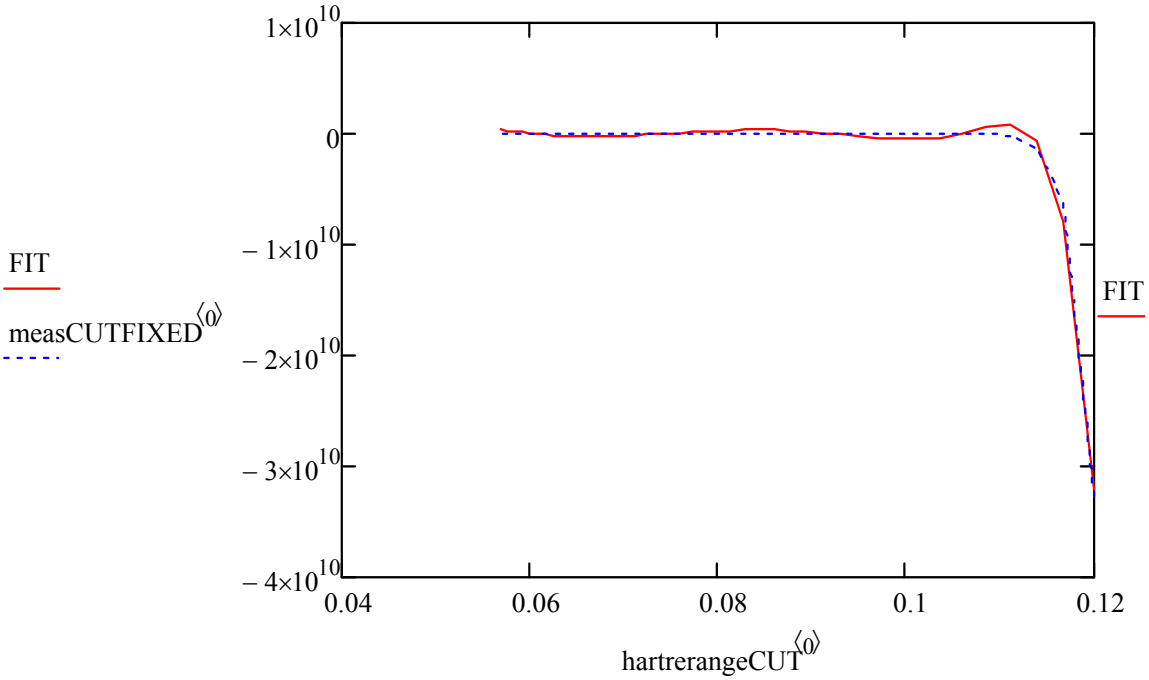

Figure 4-3 Linear fit for β_{xxx} on formaldehyde.

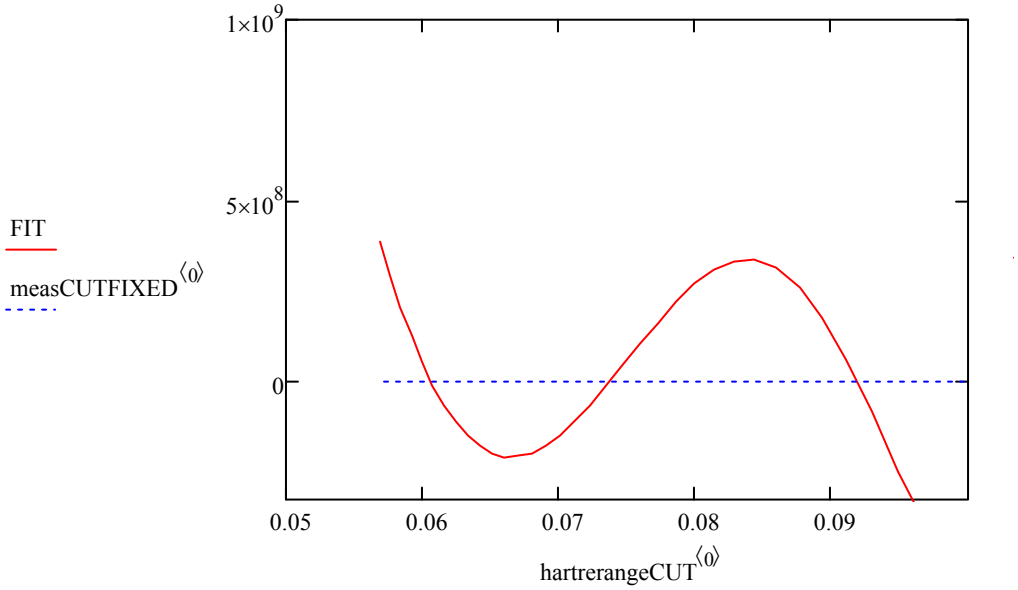

Figure 4-4 Cropped linear fit for β_{xxx} on formaldehyde.

VITA

VITA

Gregory R. Snyder was born on June 10, 1987 in Baytown, Texas to Darlene and Thomas Snyder. He attended Lutheran High School in Springfield, IL, from which he graduated in 2005. He attended Lincoln Land Community College for his first two years of undergraduate education in Springfield, IL, and finished his Bachelors in Science at the University of Kentucky in Lexington, KY, in 2009. In 2011, he moved to West Lafayette, Indiana to conduct research in Garth Simpson's research group at Purdue University, focusing on the application of computational quantum chemistry to nonlinear optics and second harming generation microscopy.